Ceramics International 48 (2022) 30640–30650

Contents lists available at ScienceDirect

Ceramics International

journal homepage: www.elsevier.com/locate/ceramint

One-pot hydrothermally prepared rGO/SiC/$CoFe_2O_4$ composites with strong microwave absorption at different thicknesses

Jiayi Wang [a], Shuhang Hu [a], Qi Tang [a], Jian Xu [a], Nianxi Xu [b], Shansheng Yu [a], Xiaoyi Wang [b,**], Hongwei Tian [a,*]

[a] Key Laboratory of Automobile Materials of MOE and School of Materials Science and Engineering, Jilin University, Changchun, 130012, China
[b] Key Laboratory of Optical System Advanced Manufacturing Technology, Changchun Institute of Optics, Fine Mechanics and Physics, Chinese Academy of Sciences, Changchun, 130033, China

ARTICLE INFO

Keywords:
Microwave absorption
Magnetic materials
Reflection loss
Reduced graphene oxide

ABSTRACT

Currently, to solve the problem of electromagnetic radiation, it is imperative to develop a thin, lightweight absorber, with a wide bandwidth and an excellent absorption ability. In this study, SiC and $CoFe_2O_4$ were combined on reduced graphene oxide (rGO) with immobilized rGO and SiC nanoparticles and varying amounts of $CoFe_2O_4$ nanoparticles. A facile one-pot hydrothermal technique was employed to prepare four rGO/SiC/$CoFe_2O_4$ composite samples with varied $CoFe_2O_4$ concentrations. The electromagnetic properties of rGO/SiC/$CoFe_2O_4$ composites were affected by $CoFe_2O_4$ content, and $CoFe_2O_4$ content was varied to change the electromagnetic properties of composites. The rGO/SiC/$CoFe_2O_4$ composite samples were prepared at a graphene oxide (GO) mass of 0.5 g, SiC mass of 0.25 g, and $CoFe_2O_4$ mass of 1.5 g, and this composite sample exhibited the best microwave absorption consumption. At 60 wt% of rGO/SiC/$CoFe_2O_4$ composite sample, the RL_{min} at 7.4 GHz with a thickness of 2.43 mm was −62.39 dB, and efficient absorption of broadband (EAB) was 1.4 GHz (6.8–8.2 GHz). The EAB was 3.2 GHz (11.8–15 GHz), and the RL_{min} was −59.77 dB at 13.2 GHz with a thickness of 1.39 mm. The RL_{min} at 17.2 GHz was −65.49 dB, and the EAB was 2.3 GHz (15.7–18 GHz), despite a thickness of only 1.06 mm. The rGO/SiC/$CoFe_2O_4$ composite comprised carbon materials, magnetic metals, and semiconductors. High-performance microwave absorption was achieved by the introduction of more than one loss mechanism and coordination and supplementation of multicomponent functions. The proposed carbon/semiconductor/magnetic composite material provides a feasible solution for the preparation of excellent microwave absorbing materials in the future.

1. Introduction

The huge software of high-power verbal exchange gear and digital units in present day society has made super contribution to the improvement and growth of society. Nevertheless, electromagnetic radiation can cause major diseases in humans, seriously hinder the normal operation of some electronic products, and lead to equipment failure. Electromagnetic radiation is a crucial problem that is difficult to deal with worldwide; hence, electromagnetic radiation is attracting increasing attention [1,2]. To solve this problem, researchers are continuously researching strong absorbing materials that can meet the demand to solve the adverse effects of electromagnetic waves. To solve the problems caused by electromagnetic wave applications, microwave absorbing materials should have characteristics such as a strong ability to consume electromagnetic waves, low thickness, and good thermal stability [3–5]. The microwave absorption capability of materials can be enhanced in terms of reflection and attenuation. The reflection and attenuation characteristics can be adjusted by the magnetic and dielectric properties, that is, changing the magnetic and dielectric properties of materials can affect their microwave absorption performance [6].

It is difficult for conventional carbon materials, metals, metal oxides, and conductive polymers to exhibit good microwave absorption capabilities due to poor impedance matching, and only a few loss mechanisms are involved in microwave absorption. As a result, practical applications of microwave absorbing materials have been considerably

* Corresponding author.
** Corresponding author.
E-mail addresses: wangxiaoyi@163.com (X. Wang), tianhw@jlu.edu.cn (H. Tian).

https://doi.org/10.1016/j.ceramint.2022.07.007
Received 26 May 2022; Received in revised form 29 June 2022; Accepted 2 July 2022
Available online 5 July 2022

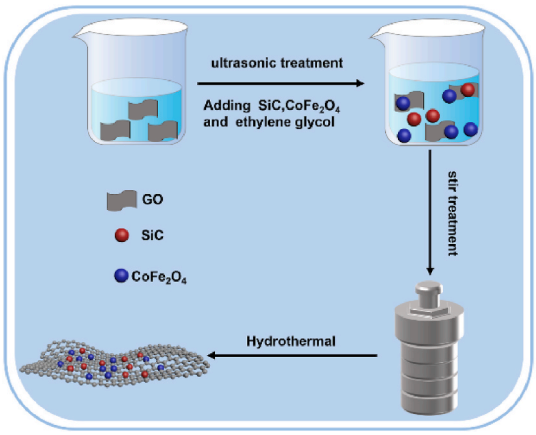

Scheme 1. Schematic of the hydrothermal synthesis route for rGO/SiC/$CoFe_2O_4$ composites.

hindered [7–10]. Clearly, the use of magnetic/dielectric composite materials is becoming an effective method to prepare excellent microwave absorbing materials. Therefore, the artificial adjustment of electromagnetic parameters for rendering excellent properties to dielectric magnetic composites has become an important research direction for the preparation of microwave absorbents [11–14]. Graphene oxide (GO) exerts a positive effect on the absorption of electromagnetic waves, and high temperatures marginally affect the performance of GO; in addition, GO has low environmental requirements, and absorbers obtained by the combination of GO flakes with magnetic materials have attracted increasing attention [15]. For instance, Huang et al. prepared an rGO aerogel with an RL_{min} of −61.63 dB and an EAB of 7.8 GHz [16]. Zhang et al. prepared a core-shell CI/SiO_2/RGO sheet with an RL_{min} of −46.43 dB and an EBA of 6.47 GHz [17].

In recent years, spinel-type transition metal oxides have been recognized for their excellent magnetic properties. Among these magnetic materials, $CoFe_2O_4$ exhibits excellent physical and chemical properties. Its magnetism is attributed to its own shape and size, which can be improved by these factors; also, it demonstrates broad application prospects in microwave absorption. However, the high density, poor high-temperature properties, and low dielectric constant of single $CoFe_2O_4$ limit its application [18]. In terms of its absorbing properties, its performance is poor, and it is challenging to fulfill the requirements for use as wave-absorbing materials. Therefore, its absorbing properties are considered to be improved by the combination of $CoFe_2O_4$ with other materials [19]. For example, Wang et al. prepared a $CoFe_2O_4$/N-doped RGO aerogel with an RL_{min} of −60.4 dB and an EAB up to 6.48 GHz (11.44–17.92 GHz) [20]. Zhu et al. prepared a polyvinylpyrrolidone-encapsulated $CoFe_2O_4$/rGO composite with an RL_{min} of −56.8 dB and an EBA of 6.8 GHz [21].

Silicon carbide (SiC) is a wide bandgap semiconductor with excellent resistance to oxidation and thermal stability as well as low density [22]. Therefore, SiC also demonstrates considerable practical utility and potential applications as microwave absorbers [23–25]. For example, Yang et al. prepared a SiC-nanowire-modified 3D printed polymer-derived SiOC ceramic with an EMI shielding efficiency of 34.7 dB [26].

In this study, rGO/SiC/$CoFe_2O_4$ composites are obtained experimentally. Scheme 1 shows the artificial route. Therefore, SiC nanoparticles and $CoFe_2O_4$ nanoparticles are combined with graphene oxide to form rGO/SiC/$CoFe_2O_4$ composites. Notably, the interaction of carbon materials, semiconductor materials, and magnetic materials via multiple loss mechanisms renders strong electromagnetic wave absorption at various thicknesses to the rGO/SiC/$CoFe_2O_4$ composites. When the rGO/SiC/$CoFe_2O_4$ composite material accounts for 60 wt% of the total content, the RL_{min} at 7.4 GHz with a thickness of 2.43 mm is −62.39 dB, and the EAB is 1.4 GHz (6.8–8.2 GHz). The EAB is 3.2 GHz (11.8–15 GHz), and the RL_{min} is −59.77 dB at 13.2 GHz with a thickness of 1.39 mm. The RL_{min} at 17.2 GHz is −65.49 dB, and the EAB is 2.3 GHz (15.7–18 GHz), despite a thickness of only 1.06 mm. These results suggest that rGO/SiC/$CoFe_2O_4$ can become high-performance microwave absorbers at one of a thin kind thicknesses. Owing to the high specific surface area and good electrical conductivity of graphene, the theoretical specific capacity of $CoFe_2O_4$ is high, and it exhibits a spinel nanostructure; its electrochemical performance is good. Owing to their complementary electrochemical windows, graphene and $CoFe_2O_4$ can only be used as positive and negative electrodes, respectively, for asymmetric supercapacitors. The rGO/SiC/$CoFe_2O_4$ material demonstrates potential for application in supercapacitors [27–29].

2. Experiment

2.1. Materials

SiC was purchased from Aladdin Reagent (Shanghai) Co., Ltd., cobalt ferrite ($CoFe_2O_4$) was purchased from Shanghai Maclean Biochemical Technology Co., Ltd., graphene oxide (GO) was purchased from Hangzhou Hangdan Optoelectronics Technology, and ethylene glycol purchased from China Sinopharm Chemical Reagent Co., Ltd. Deionized water was used during the experiment.

2.2. Synthesis of rGO/SiC/$CoFe_2O_4$ composites

A simple method was employed to synthesize rGO/SiC/$CoFe_2O_4$ composites. First, 0.5 g of GO was transferred to 165 mL of deionized water, which was poured into a beaker, and then it was sonicated for 2 h to fully disperse it. Next, 200 mL of ethylene glycol, 0.25 g of SiC, and $CoFe_2O_4$ were added to the aqueous graphene solution that had been

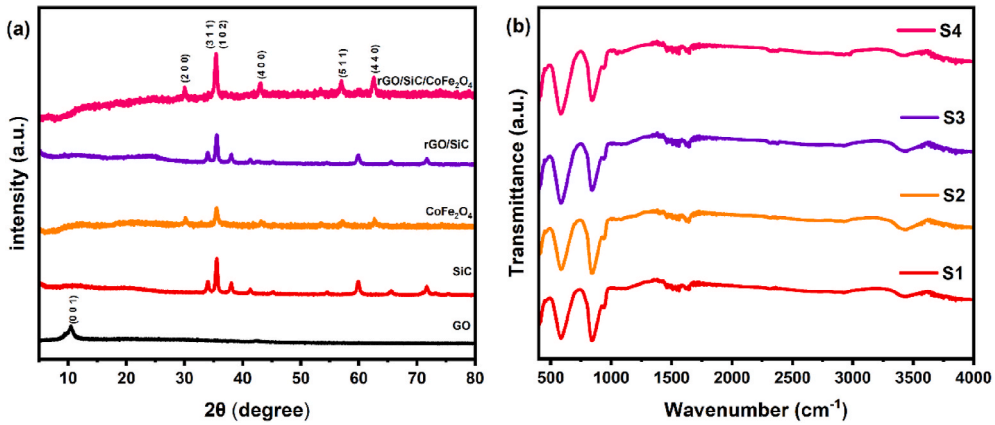

Fig. 1. XRD patterns of GO, SiC, $CoFe_2O_4$, rGO/SiC, and rGO/SiC/$CoFe_2O_4$ (a), FTIR spectra of samples S1, S2, S3, and S4 (b).

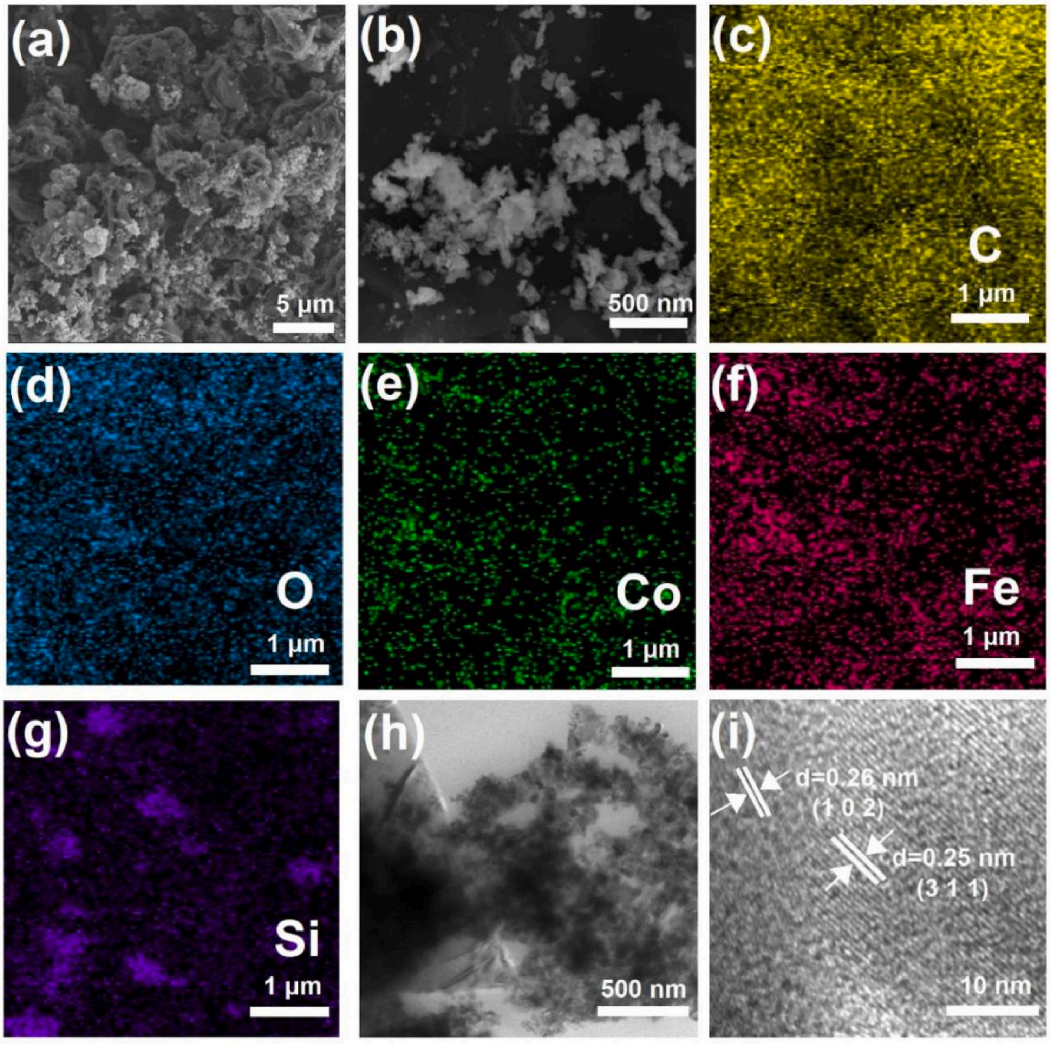

Fig. 2. SEM images of S3 (a–b), EDS elemental mapping of C, O, Co, Fe, and Si in sample S3 (c–g), TEM image of S3 (h), HRTEM image of S3 (i).

dispersed above, and ultrasonic treatment was continued for 1 h, followed by stirring the dispersed solution for 1 h with a stirrer to ensure thorough mixing of all components in the solution. The already mixed substances were shifted to a reaction kettle. The temperature and time of the hydrothermal reaction were set at 200 °C and 12 h, respectively. After the reaction was completed, the reaction kettle was allowed to cool, and the product was collected and centrifuged several times with alcohol. Finally, the centrifuged samples were vacuum dried at 65 °C for 10 h, affording the ultimate composite sample. Four samples were prepared with the increase in the $CoFe_2O_4$ content, i.e., S1, S2, S3, and S4, respectively, with corresponding $CoFe_2O_4$ contents of 1.0, 1.25, 1.5, and 1.75 g.

2.3. Characterization

Phase and crystallinity of the samples were characterized by X-ray diffraction (XRD, Bruker, D8 Advance) with CuKα radiation and λ = 1.5406 Å. Chemical bonds and atoms were analyzed by X-ray photoelectron spectroscopy (XPS, Escalab-250 X-ray). Micromorphological examination and elemental composition were analyzed by scanning electron microscopy (SEM, Hitachi SU8010) and transmission electron microscopy (TEM, JEOL JEM-2100f). The chemical composition was analyzed by Fourier transform infrared (FTIR, Thermo Fisher Scientific Nicolet 6700) spectroscopy. The surface areas of the powders were analyzed by a Gemini VII analyzer. Magnetic properties were measured by using a magnetic measurement system (VSM, Lakeshore7407). Electromagnetic parameters were measured by a vector network analyzer (Agilent, N5234A). The content of composites was examined by thermogravimetric analysis (TGA, TGA1150).

3. Results and discussion

3.1. Composition, Micromorphology, and magnetic properties

The crystal structure and crystallinity were determined by XRD (Fig. 1(a)). From the XRD pattern of GO, a diffraction peak is observed at 2θ = 10.74°, attributed to the (0 0 1) crystal plane of GO. SiC exhibits seven diffraction peaks at 2θ values of 33.96°, 35.56°, 38.06°, 41.28°, 59.90°, 65.56°, and 71.86°, corresponding to the (1 0 1), (1 0 2), (1 0 3), (1 0 4), (1 1 0), (1 0 9), and (1 1 6) crystal planes of SiC, respectively. $CoFe_2O_4$ exhibits five diffraction peaks at 2θ values of 30.12°, 35.54°, 43.74°, 57.24°, and 62.66°, corresponding to the (2 2 0), (3 1 1), (4 0 0), (5 1 1), and (4 4 0) planes of $CoFe_2O_4$, respectively. In the XRD pattern of the rGO/SiC/$CoFe_2O_4$ composite material, all characteristic peaks of $CoFe_2O_4$ and some characteristic peaks of SiC are observed. The results revealed that the crystal structure is not changed by the addition of graphene. As GO is shown to be reduced to rGO, only the peaks of $CoFe_2O_4$ and SiC are observed, and the diffraction peaks attributed to GO disappear. Other peaks are not observed, indicating that high-purity rGO/SiC/$CoFe_2O_4$ is prepared [30,31].

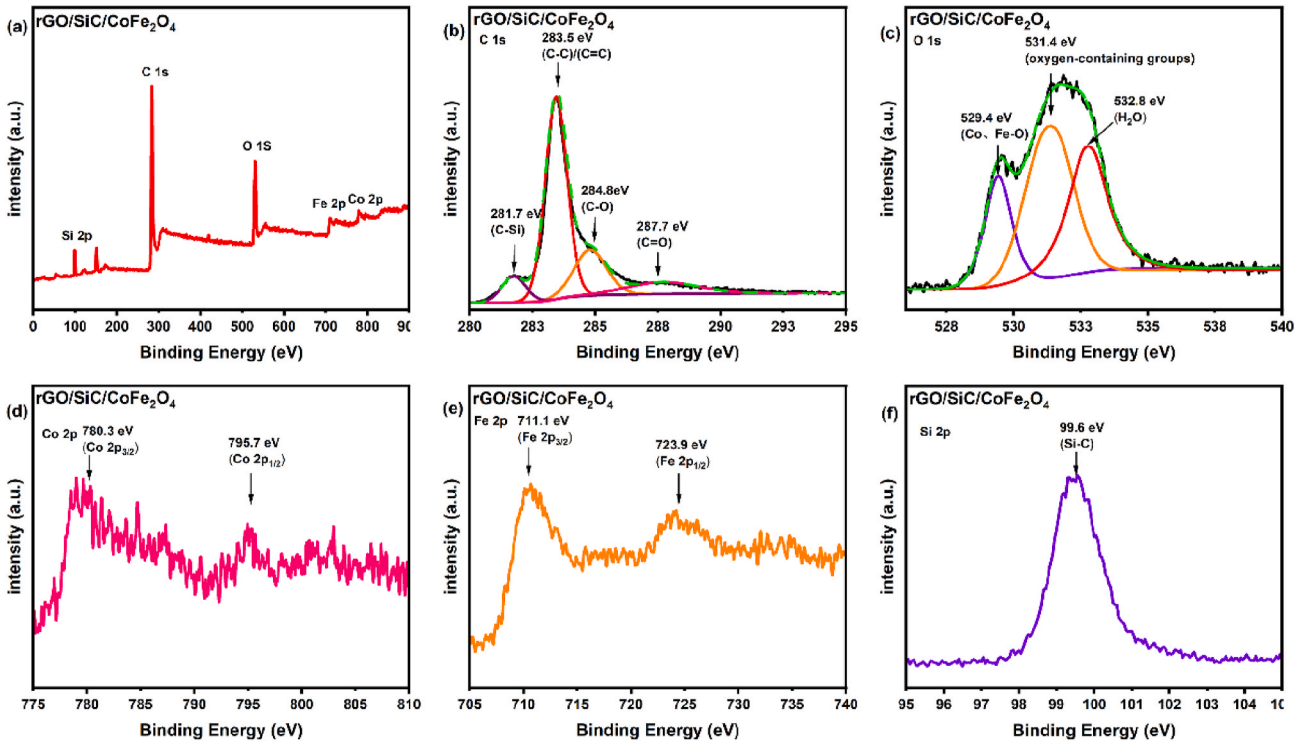

Fig. 3. XPS spectra: wide scan (a), C 1s spectrum (b), O 1s spectrum (c), Co 2p spectrum (d), Fe 2p spectrum (e), Si 2p spectrum of sample S3 (f).

A clear absorption peak at 577 cm^{-1} is observed in the IR spectrum (Fig. 1(b)), corresponding to FeO_6 metal bond vibrations; this result indicates that $CoFe_2O_4$ is present in the composite sample. A clear absorption peak corresponding to the Si–C of SiC at 841 cm^{-1} is observed, indicative of the presence of SiC in the composite sample. The C–O–C vibration is related to the absorption peak at 1110 cm^{-1}, the C–OH bending vibration is related to the absorption peak at 1630 cm^{-1}, the C═O stretching vibration is related to the absorption peak at 1750 cm^{-1}, and the OH stretching vibration is related to the absorption peak at 3430 cm^{-1}. The presence of rGO in the composite sample is confirmed by the absorption peak. The above analysis revealed the successful preparation of the rGO/SiC/$CoFe_2O_4$ composite [32,33].

To investigate the morphology of the prepared composite material, a representative sample S3 was used for SEM (Fig. 2(a and b)), SEM-EDS (Fig. 2(c–g)), and TEM (Fig. 2(h–i)) tests. Owing to the deformation during peeling and re-stacking, the rGO sheet exhibits a wrinkled

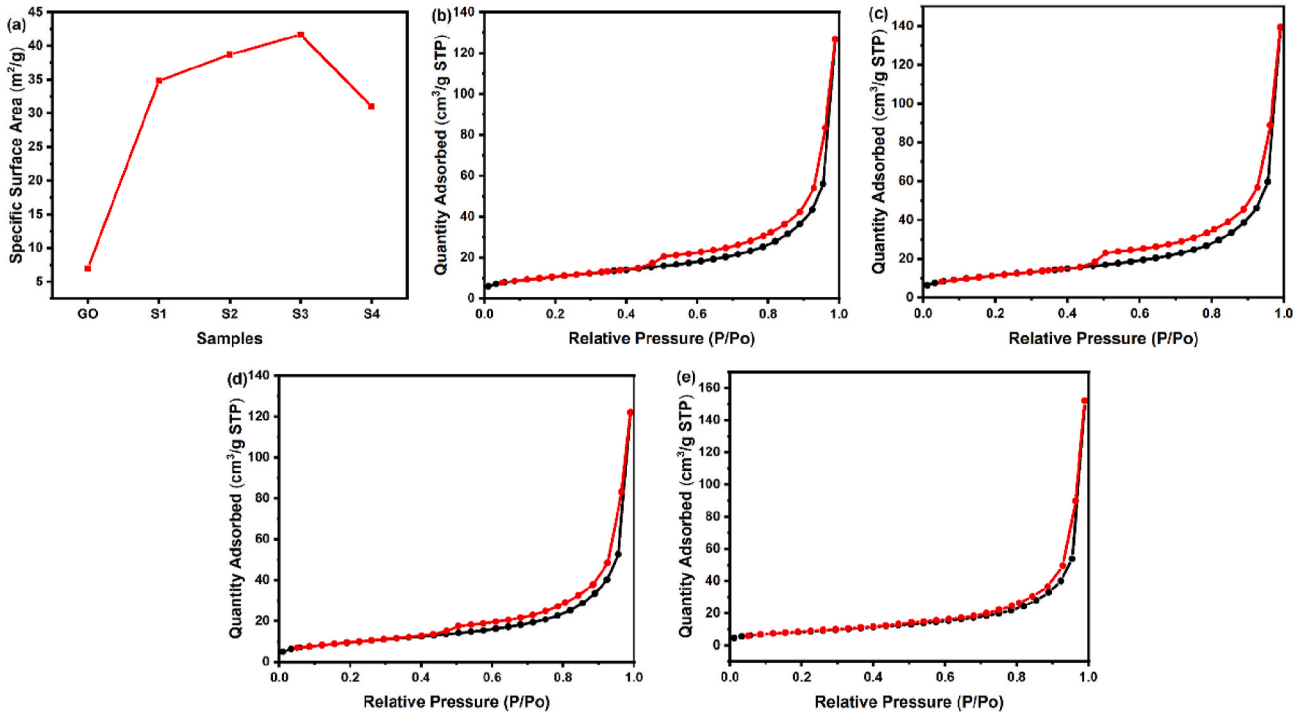

Fig. 4. Specific surface areas of GO and samples S1, S2, S3, and S4 (a), N_2 adsorption–desorption isotherms of samples S1, S2, S3, and S4 (b–e).

Table 1
Specific surface area and pore volume of GO and all samples.

Sample	GO	S1	S2	S3	S4
S_{BET} (m^2/g)	6.99	34.81	38.71	41.65	30.99
Pore volumes (cm^3/g)	0.022	0.189	0.196	0.215	0.233

corrugated structure. A large number of regular spherical $CoFe_2O_4$ nanoparticles and SiC nanoparticles adhere tightly to the rGO sheet surface. In addition, the distribution of $CoFe_2O_4$ on the rGO surface is observed from the EDS elemental mapping results, and $CoFe_2O_4$ is evenly scattered on the rGO surface [34,35]. The TEM image suggests that $CoFe_2O_4$ nanoparticles and SiC nanoparticles are immobilized on the rGO nanosheet surface. Although $CoFe_2O_4$ is sonicated during TEM sample preparation, $CoFe_2O_4$ particles are still attached to rGO, indicative of a good adhesion force between rGO and $CoFe_2O_4$ and SiC. The successful synthesis of the rGO/SiC/$CoFe_2O_4$ composite sample is further demonstrated by the following factors. A lattice fringe with a 0.25-nm interplanar spacing is observed because of the (3 1 1) plane of $CoFe_2O_4$, and a lattice fringe with a 0.26-nm interplanar spacing is observed because of the (1 0 2) plane of SiC, confirming the existence of $CoFe_2O_4$ and SiC in the sample [36].

The chemical bonds of rGO/SiC/$CoFe_2O_4$ composites were determined by XPS spectra (Fig. 3) of representative sample S3. The elemental composition of the composite rGO/SiC/$CoFe_2O_4$ was determined from the wide-scan XPS spectrum (Fig. 3(a)). C, O, N, Fe, Co, and Si are present in the composite sample rGO/SiC/$CoFe_2O_4$. High-resolution C 1s, O 1s, Fe 2p, Co 2p, and Si 2p XPS spectra (Fig. 3(b–f)) were recorded. Fig. 3(b) reveals that C–Si, C–C, C–O, and C═O are the four main components, respectively, with corresponding binding energies of 281.7, 283.5, 284.8, and 287.7 eV. Notably, compared with previously reported GO, the peak strength of the C–O bond in the rGO/SiC/$CoFe_2O_4$ composite is weaker, indicating that GO is significantly reduced. Furthermore, sp^2 bonds of carbon atoms account for the major proportion of non-synthetic components, which is verified from the peak at 283.5 eV. The O 1s spectrum reveals the presence of $CoFe_2O_4$, oxygen-containing groups, and water molecules in the composite sample, and the O of $CoFe_2O_4$, oxygen-containing groups, and water molecules correspond to the three peaks observed in the XPS spectrum at 529.4, 531.4 and 532.8 eV, respectively. The Co 2p XPS spectrum reveals that Co is confirmed to be present in the sample, and peaks at 780.3 and 795.7 eV confirm the presence of Co^{2+}. The Fe 2p XPS spectrum reveals that Fe exists in the composite sample and that peaks at 711.1 and 723.9 eV demonstrate the presence of Fe. The Si 2p spectrum reveals that Si exists in the composite sample and that the characteristic peak corresponding to Si–C is observed at 99.6 eV. According to the above analysis, the rGO/SiC/$CoFe_2O_4$ composite sample is successfully synthesized [37,38].

The S_{BET} values of samples S1, S2, S3, and S4 are plotted (Fig. 4(a)), where the S_{BET} of pure GO is 6.99 m^2/g. With the increase in the $CoFe_2O_4$ amount, the S_{BET} of rGO/SiC/$CoFe_2O_4$ composites increases. The S_{BET} value of S3 (41.65 m^2/g) is the highest. In addition, the pore size distribution and pore volume were measured. The mesoporous structure of the sample is evidence for the Type IV adsorption isotherm (Fig. 4(b–e)). The microwave absorption performance is affected by the specific surface area and porosity. When electromagnetic waves enter the sample, they are reflected and scattered at the surface. Therefore, microwave and energy absorption are improved when S_{BET} and porosity are high [39–41]. S_{BET} and pore volume values are listed in Table 1.

To determine the species content of the samples, TGA of GO and a representative sample S3 was performed under N_2. TGA curves are plotted from 40 to 800 °C (Fig. 5(a)). A weight loss of ~7% at 100 °C corresponding to the evaporation of H_2O is observed. At 100–400 °C, the elimination of unstable oxygen-containing functional groups causes a weight loss of ~45%. The graphene structure and stable oxygen-containing functional groups then decompose at high temperatures, resulting in a considerable weight loss from 400 to 800 °C. In the TGA curve of the representative sample S3, SiC and $CoFe_2O_4$ are not easily decomposed at high temperatures, and the residual weight of sample S3 is mainly distributed to SiC and $CoFe_2O_4$ in the composite material. Here, relative weights of SiC and $CoFe_2O_4$ in sample S3 are about 82 wt %, confirming the composition of sample S3 [42–44].

The hysteresis loops of the samples are plotted (Fig. 5(b)). The saturation magnetization (M_s) values for all samples are 37.3, 39.9, 39.0, and 39.7 emu/g, respectively. The corresponding saturation magnetization of rGO/SiC/$CoFe_2O_4$ composites is independent of the $CoFe_2O_4$ content, and the M_s of the composites hardly changes despite the increase in the $CoFe_2O_4$ content.

3.2. Electromagnetic wave absorption ability

Generally, the microwave absorption property of the sample can be obtained by the transmission line theory, which can be expressed by RL. The formula of RL is as follows: Equation (1) and Equation (2).

$$RL = 20log\left|\frac{Z_{in} - Z_0}{Z_{in} + Z_0}\right| \quad (1)$$

$$Z_{in} = Z_0\sqrt{\frac{\mu_r}{\varepsilon_r}}tanh\left[j\left(\frac{2\pi fd}{c}\right)\sqrt{\mu_r\varepsilon_r}\right] \quad (2)$$

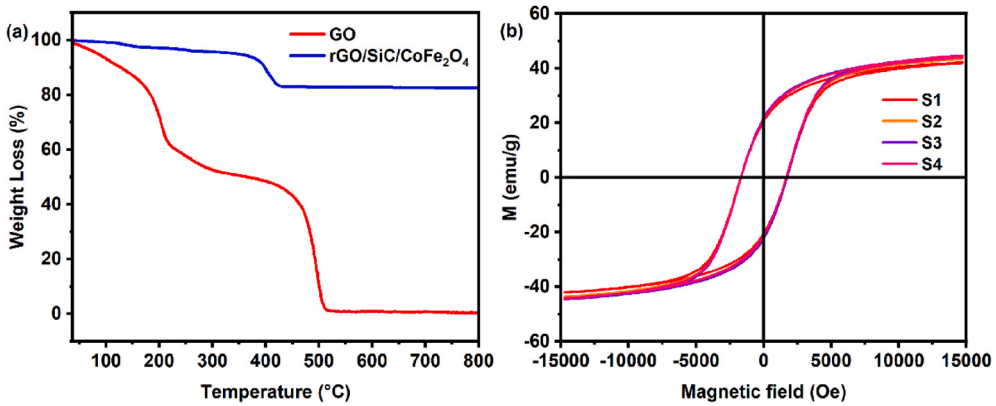

Fig. 5. TGA curves of samples GO and rGO/SiC/$CoFe_2O_4$ (a), room-temperature hysteresis loop of samples S1, S2, S3, and S4 (b).

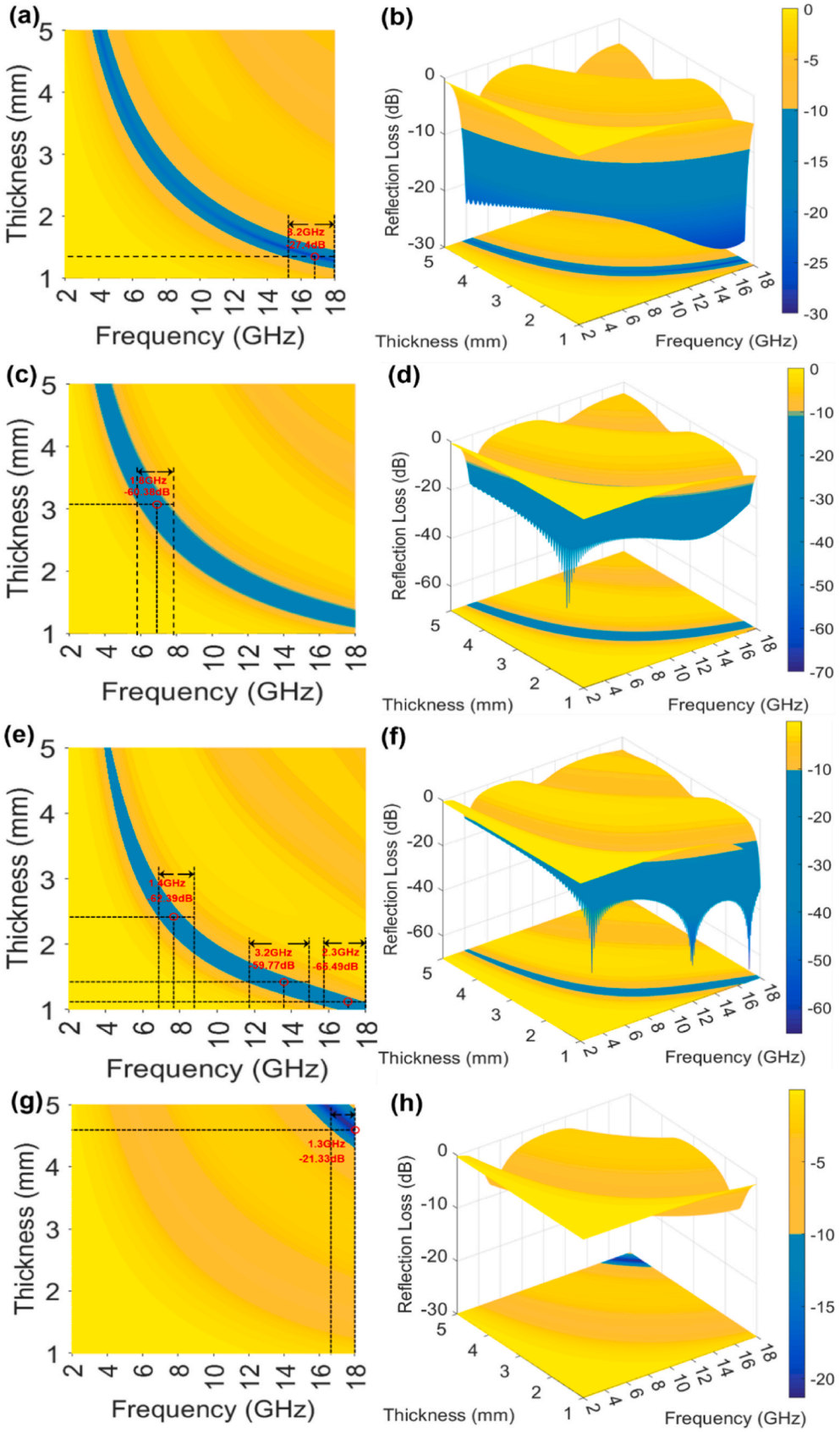

Fig. 6. 2D image of reflection loss versus frequency for S1 (a), S2 (c), S3 (e), S4 (g), the corresponding 3D contour maps of reflection loss versus frequency and thickness for S1 (b), S2 (d), S3 (f), S4 (h).

Table 2
Comparison of some RL_{min} values, EAB, and matching thickness of graphene-based microwave absorbers reported previously.

Sample	RL_{min} (dB)	Thickness (mm)	EAB (GHz)	Refs.
$CoFe_2O_4$/rGO	−57.7	1.7	5.8	[65]
rGO/$CoFe_2O_4$	−50.0	2.3/2.0	6.16	[59]
$CoFe_2O_4$/rGO/SiO_2	−24.8	2.0	1.7	[66]
Ni@Co_3O_4/RGO	−60.0	2.3	4.62	[47]
Fe_3O_4/rGO	−50.2	1.5	4.1	[67]
SiC_f/SiC_{nw}/Si_3N_4	−51.4	3.2	3.5	[68]
rGO/SiC/$CoFe_2O_4$	−62.39	2.43	1.4	this study
	−59.77	1.39	3.2	this study
	−65.49	1.06	2.3	this study

where Z_{in}, Z_0, ε_r, μ_r, f, d, and c are the normalized input impedance, free-space impedance, relative complex permittivity, relative complex permeability, microwave frequency, absorber thickness, and microwave velocity of the absorber, respectively. Generally, the microwave absorption capability is inversely proportional to RL. Then, the EAB refers to the range of RL < −10 dB. When RL < −10 dB, the microwave absorption can be as high as 90% [45–47].

The RL values at 2–18 GHz for all samples at a 60 wt% filler loading are plotted (Fig. (6)). The RL value of sample S1 is plotted (Fig. 6(a and b)). The EAB is 3.2 GHz (14.8–18 GHz), while the RL_{min} value at 16.7 GHz with a thickness of 1.36 mm is just −27.40 dB. Fig. 6(c and d) shows the RL value of sample S2: The EAB is 1.8 GHz (5.9–7.8 GHz) and the RL_{min} is −60.38 dB at 6.7 GHz with a thickness of 3.03 mm. The optimum microwave absorption property for sample S3 is shown. Fig. 6(e and f) shows the RL values of sample S3: the RL_{min} at 7.4 GHz with a thickness of 2.43 mm is −62.39 dB, and the EAB is 1.4 GHz (6.8–8.2 GHz). The EAB is 3.2 GHz (11.8–15 GHz), and the RL_{min} is −59.77 dB at 13.2 GHz with a thickness of 1.39 mm. The RL_{min} at 17.2 GHz is 65.49 −dB, and the EAB is 2.3 GHz (15.7–18 GHz), despite a thickness of only 1.06 mm. Fig. 6(g and h) shows the RL value of sample S4: The EAB is 1.3 GHz (16.7–18 GHz), and the RL_{min} is −21.33 dB at 18 GHz with a thickness of 4.95 mm. The synthesized sample S3 exhibits clear advantages, and it is predicted to be a new absorbing material (see Table 2).

The basic microwave absorption mechanism can be revealed by the following four factors: relative complex permittivity ($\varepsilon_r = \varepsilon' j\varepsilon''$) includes real and imaginary parts, representing storage and consumption, respectively. Relative complex permeability ($\mu_r = \mu$ 'jμ") includes real and imaginary parts, representing storage and consumption, respectively. The dielectric loss tangent tanδε ($\tan\delta_\varepsilon = \varepsilon''/\varepsilon'$) represents the dielectric loss factor. The magnetic loss tangent tanδμ ($\tan\delta_\varepsilon = \mu''/\mu'$) represents the magnetic loss factor (Fig. 7) [48]. The ϵ' and ϵ'' values versus frequency in all samples are plotted (Fig. 7(a and b)). Notably, with the increase in the $CoFe_2O_4$ amount, ϵ' and ϵ'' values first increase and then decrease. The changes in μ′ and μ'' with frequency in all samples are plotted (Fig. 7(c and d)). In addition, with the continuous increase in the $CoFe_2O_4$ content, the μ′ of the sample is nearly unchanged typically; however, the μ'' of the sample first increases and then decreases. $\tan\delta_\varepsilon$ and $\tan\delta_\mu$ are shown in Fig. 7(e and f). The impedance matching characteristics of the absorber are related to the dielectric dissipation factor. When the dielectric dissipation factor is high (>0.5), the impedance matching characteristics are not extremely good. The $\tan\delta_\epsilon$ of all samples is less than 0.5. Clearly, because good impedance-impedance matching can enhance the microwave absorption ability, impedance matching is concurrently affected via dielectric loss and magnetic loss. The microwave loss of the sample is more often than not caused with the assistance of dielectric loss, because $\tan\delta_\epsilon$ is greater than $\tan\delta_\mu$ [49,50].

Generally, microwave absorbing materials exhibit two losses, conduction loss and polarization loss, respectively, which are the essential components of the dielectric loss. From the free electron theory, the free-electron theoretical formula is expressed as $\varepsilon'' \approx \sigma/2\pi\varepsilon_0 f$, where σ and ε_0 are the conductivity and permittivity in vacuum, respectively. Therefore, ε" is related to conductivity and ε" is proportional to conductivity. The higher the conductivity, the higher the ε" value. In addition, owing to the unique fold structure of the sample, the microwaves entering the sample are rapidly captured by the internal space, resulting in long multiple reflections and a diffuse scattering period [51–53]. As mentioned above, the addition of rGO and semiconductor SiC to the composite material can easily render high conductivity and improve complex permittivity. A large amount of $CoFe_2O_4$ and SiC

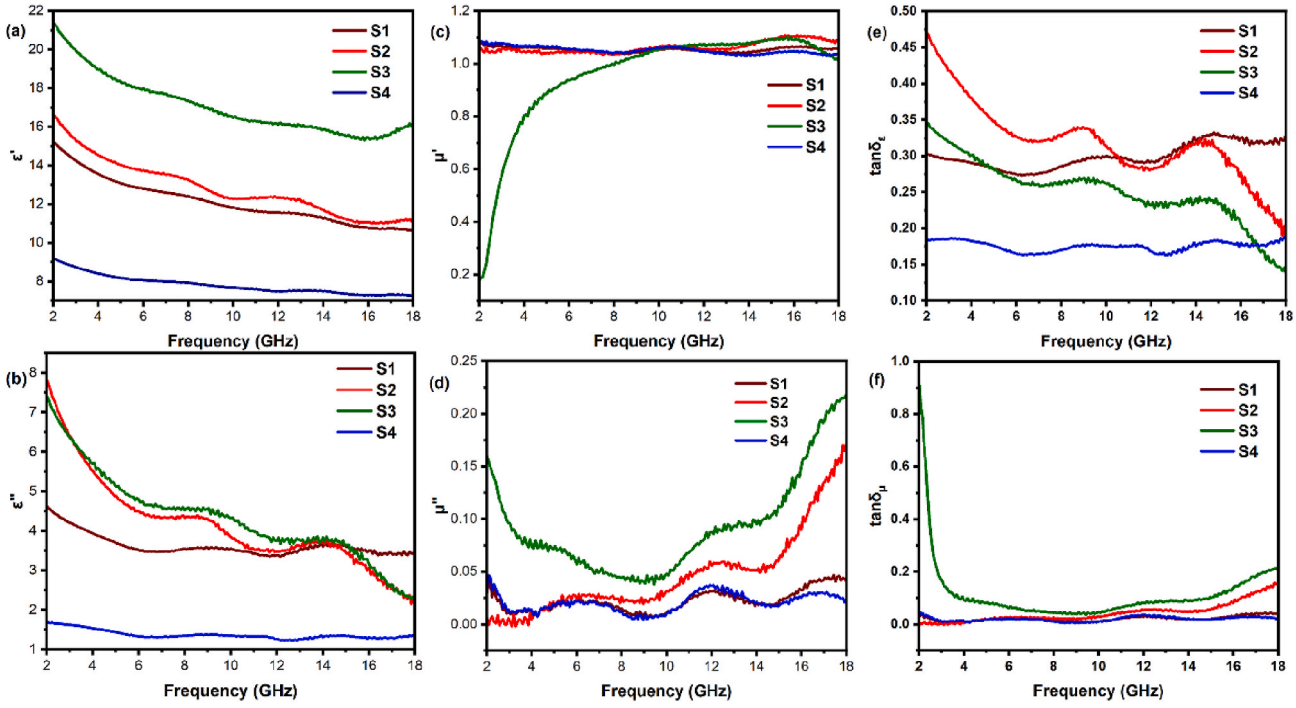

Fig. 7. Frequency dependence of the real part of permittivity (a), frequency dependence of the imaginary part of permittivity (b), frequency dependence of the real part of permeability (c), frequency dependence of the imaginary part of permeability (d), dielectric loss tangent $\tan\delta_\varepsilon$ (e), magnetic loss tangent $\tan\delta_\mu$ (f).

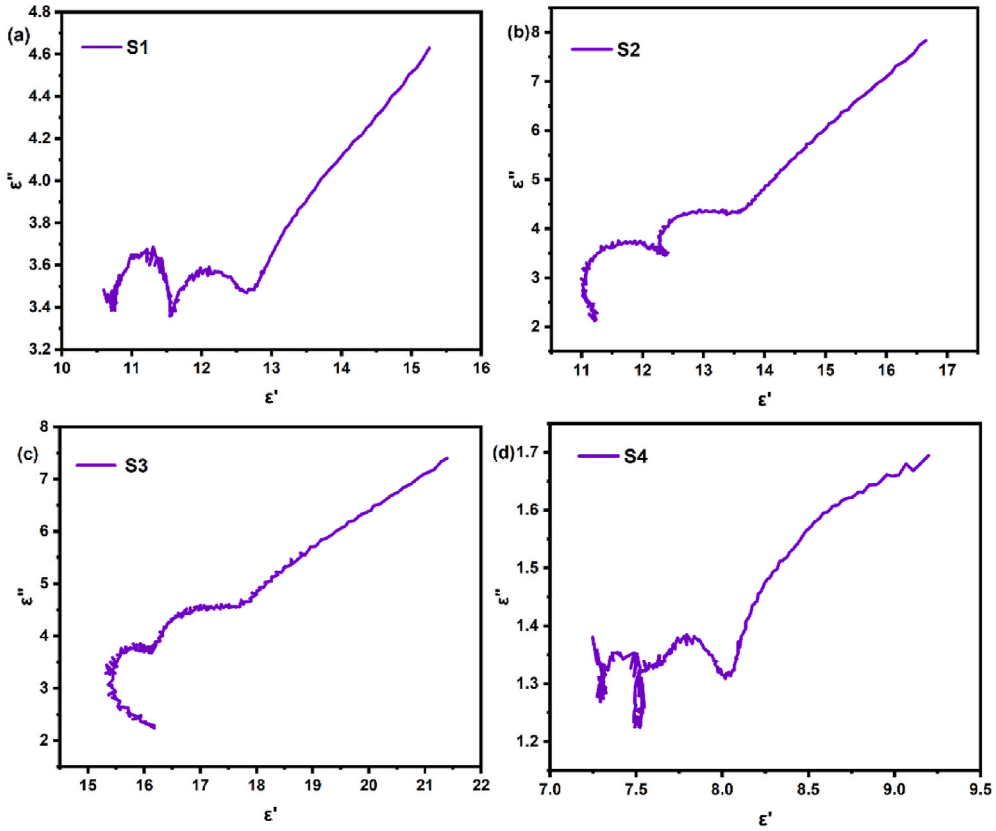

Fig. 8. Cole-Cole semicircle of samples S1 (a), S2 (b), S3 (c), S4 (d).

nanoparticles are turbidly dispersed in the rGO flakes, forming an effective conductive network structure, thereby resulting in considerable physical contact between rGO and $CoFe_2O_4$ and SiC nanoparticles. Then, the conduction loss of rGO/SiC/$CoFe_2O_4$ composites is enhanced by the increase in electrical conductivity. The resistance in samples can effectively dissipate the current generated by induction; hence, electric energy is reduced into heat energy. As mentioned above, defect polarization relaxation and electron dipole relaxation produced in the sample are caused by the residual groups and defects contained in rGO when microwaves penetrate rGO/SiC/$CoFe_2O_4$ composites. In addition, the interfacial polarization generated in the sample at the interface is caused by the existence of considerably different interfaces between $CoFe_2O_4$ and SiC nanoparticles and rGO flakes, where a large amount of interface leads to charge accumulation, which is conducive to increasing the polarization loss of incident microwaves [54,55]. The Cole-Cole semicircle is now used to delineate the relaxation process, as suggested by the Debye relaxation theory, with a separate semicircle representing the Debye relaxation process. A semicircle can be expressed here by the relationship between ε′ and ε", which is written as: Equation (3).

$$\left(\varepsilon' - \frac{\varepsilon_s + \varepsilon_\infty}{2}\right)^2 + (\varepsilon'')^2 = \left(\frac{\varepsilon_s - \varepsilon_\infty}{2}\right)^2 \quad (3)$$

where ε_s is the static dielectric constant, and ε_∞ is the dielectric constant at an infinite frequency. The ε′–ε" curves of all samples are plotted (Fig. 8 (a–d)). Multiple Debye relaxation processes in each sample can be represented by each semicircle drawn by the sample. Notably, the number of semicircles in the sample is related to the content of $CoFe_2O_4$ in the composite, and the number of semicircles is proportional to the content

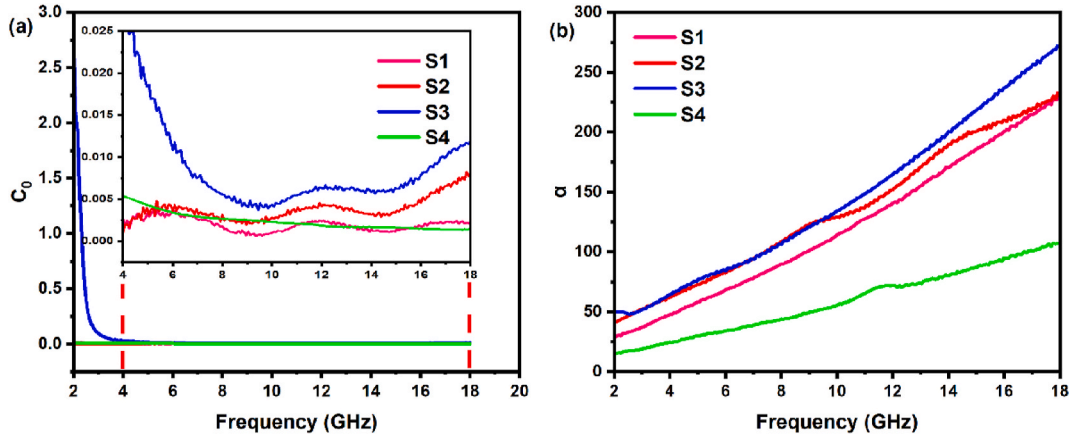

Fig. 9. C_0–f curves of samples S1, S2, S3, and S4 (a), attenuation constant α of samples S1, S2, S3, and S4 (b).

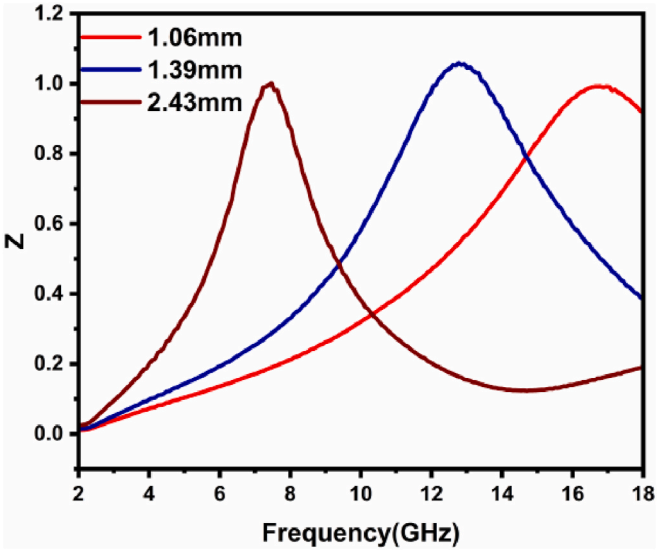

Fig. 10. Normal characteristic impedance Z of S3 samples at 1.06 mm, 1.39 mm, and 2.43 mm thicknesses.

of $CoFe_2O_4$ in the composite. In other words, with the increase in the $CoFe_2O_4$ content, the number of semicircles in sample S4 is greater than that in the other three samples, indicating that the polarization of defects or chemical bonds occupies a large proportion of the dielectric loss of the samples involving the interface. The higher the number of irregular semicircles in sample S4, the higher the number of interfaces, defects, and chemical bonds; hence, polarization loss in each sample is confirmed. In addition, a long tail is observed in all sample curves due to conduction losses, indicating that polarization and conduction losses are involved in the dielectric loss of the samples [56–58].

In most cases, natural resonance, exchange resonance, and eddy current loss are the three mechanisms that contribute to the primary composition of magnetic loss, and different mechanisms participate in magnetic loss at different frequencies. At low frequencies, natural resonance is the predominant source of magnetic loss, whereas at high frequencies, exchange resonance is the primary source of magnetic loss. C_0 ($C_0 = \mu''(\mu')^{-2}f^{-1}$) does not reach a constant value when eddy current loss outweighs magnetic loss. The C_0-f curves for all samples are shown in Fig. 9(a). At 2–7 GHz, clear resonance peaks are detected, suggesting that natural resonance is the magnetic loss mechanism at low frequencies, demonstrating that the primary mechanisms are eddy current loss and exchange resonance and that the exchange resonance is the key mechanism and participates in the magnetic loss of samples S1, S2, and S3 at high frequencies. At high frequencies, the eddy current loss among the three mechanisms is the main participating mechanism for the magnetic loss of the S4 sample [59].

Furthermore, the incident electromagnetic wave's attenuation significantly impacts a change in the attenuation constant. The attenuation constant, which can be stated by the following formula, reflects the absorber's dissipation properties and total attenuation capability: Equation (4).

$$\alpha = \frac{\sqrt{2}\pi f}{c}\sqrt{(\mu''\varepsilon'' - \mu'\varepsilon') + \sqrt{(\mu''\varepsilon'' - \mu'\varepsilon')^2 + (\mu''\varepsilon'' + \mu'\varepsilon')^2}} \quad (4)$$

Fig. 9(b) shows the computed decay constants S1–4 of the synthesized samples. In the range of 2–18 GHz, the values of all samples increase monotonically. Furthermore, for S1, the frequency shifts from 27.8 GHz to 227.5 GHz at 18 GHz. As a result, S2 and S3 values increase from 40.8 to 232.6 and 49.7 to 271.8, respectively. Notably, at a given frequency, the values are rigidly ordered according to the microwave absorption capacity distribution (S3 > S2 > S1 > S4), and the complex permittivity changes shown in Fig. 7(a)–(b) indicate that the change in

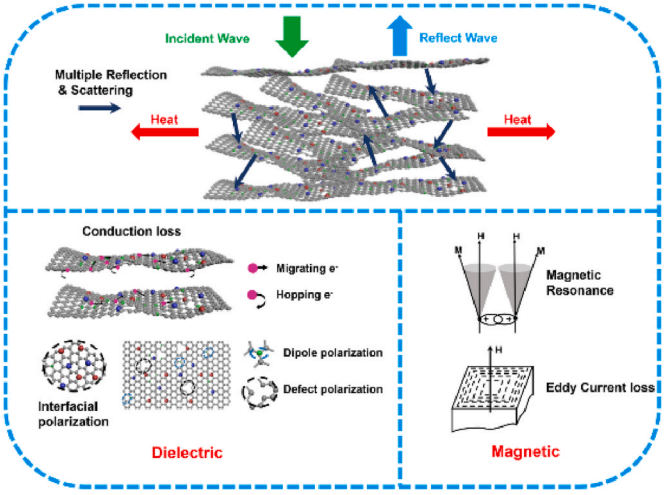

Fig. 11. Schematic of the microwave absorption principle of the rGO/SiC/$CoFe_2O_4$ composite material.

the α value is also reflected in the dielectric loss tangent in Fig. 7(e). The α value exhibits a clear relationship with the complex permittivity and dielectric loss tangent. From the above phenomenon, the dissipation of electromagnetic energy caused by dielectric loss accounts for the main part of the total electromagnetic consumption. Here, S3 exhibits the best attenuation ability; hence, S3 exhibits the best microwave absorption ability [60,61].

In fact, the normalized impedance matching Z is the main parameter to measure the microwave absorption performance of the absorber. Therefore, according to transmission line theory, Z can be expressed as: Equation (5).

$$Z = \left|\frac{Z_{in}}{Z_0}\right| = \left|\sqrt{\frac{\mu_r}{\varepsilon_r}}tanh\left[j\left(\frac{2\pi fd}{c}\right)\sqrt{\mu_r\varepsilon_r}\right]\right| \quad (5)$$

where Z_{in} is the absorber's normalized input impedance, and Z_0 is the free space impedance. When Z = 1, the microwave absorber's characteristic impedance is equal to or similar to the characteristic impedance of empty space, allowing incident electromagnetic waves to enter the absorber more easily. After further conversion of the input electromagnetic wave into thermal energy, an excellent microwave absorption capability is attained. Fig. 10 shows the computed Z-values for S3 in the 2–18 GHz frequency range at 1.06 mm, 1.39 mm, and 2.43 mm. Z is close to 1 when microwave consumption is optimal, as shown.

According to the above analysis, the following factors are accountable for the strong electromagnetic wave absorption ability of rGO/SiC/$CoFe_2O_4$ composites (Fig. 11). (1) The abundant interfacial features between rGO, $CoFe_2O_4$, and SiC and the wrinkled structure of graphene result in the reflections and scattering occurring in the rGO/SiC/$CoFe_2O_4$ composite during the propagation of the incident microwaves; the existence of a porous conductive network is helpful to growing conduction loss in rGO/SiC/$CoFe_2O_4$ composites. The accumulation of bound charges at the junction leads to the attenuation of the electromagnetic wave, and the polarization at the interface also participates in the attenuation of the electromagnetic wave [62]. (2) In rGO/SiC/$CoFe_2O_4$ composites, a traditional conductive network is observed, as well as functional groups and defects. In the rGO/SiC/$CoFe_2O_4$ system's conductive network of graphene layers, $CoFe_2O_4$ and SiC are used as an insulator and a wide bandgap semiconductor, respectively. Because of the rGO/SiC/$CoFe_2O_4$ resistance, rGO/SiC/$CoFe_2O_4$ can take up considerable electric power. Besides, when microcurrents are conveyed to $CoFe_2O_4$, a small part of the current is weakened by graphene. The conduction loss of the GO/SiC/$CoFe_2O_4$ composite is increased by the composite structure. In addition, the charge distribution, dipole polarization, and relaxation also vary because of the surface structure of the

composites. (3) Good impedance matching characteristics. Notably, the ability of impedance matching and microwave absorption is affected by the synergistic effect of dielectric loss and magnetic loss, and a good synergistic effect can provide ideal impedance matching and an enhanced microwave absorption ability. The dielectric and magnetic properties and microwave absorption properties of rGO/SiC/$CoFe_2O_4$ are affected by the aforementioned dipole polarization, interfacial polarization, Debye relaxation, eddy current loss, loss after synthesis of natural and exchange resonances, multiple reflections and scattering effect characteristics, and other factors; these factors help to further develop the microwave absorption capacity of the S1 sample [63,64].

4. Conclusions

In conclusion, rGO/SiC/$CoFe_2O_4$ was smoothly synthesized by a simple hydrothermal process, and the synthesized rGO/SiC/$CoFe_2O_4$ composite exhibited robust properties. Sample S3 outperformed other samples. Here, the RL_{min} at 7.4 GHz with a thickness of 2.43 mm was −62.39 dB, and the EAB was 1.4 GHz (6.8–8.2 GHz). The EAB was 3.2 GHz (11.8–15 GHz), and the RL_{min} was −59.77 dB at 13.2 GHz with a thickness of 1.39 mm. The RL_{min} at 17.2 GHz was −65.49 dB, and the EAB was 2.3 GHz (15.7–18 GHz), despite a thickness of only 1.06 mm. The experimental result reveals that the strong electromagnetic wave absorption capability of rGO/SiC/$CoFe_2O_4$ is caused by synergy between the increased dielectric loss, good impedance matching, and attenuation constant. Therefore, our study proposes a carbon/semiconductor/magnetic composite material to increase the wave absorbing ability and provides an advanced idea.

Declaration of competing interest

The authors declare that they have no known competing financial interests or personal relationships that could have appeared to influence the work reported in this paper.

Acknowledgements

This study was financially supported by the International Science and Technology Cooperation Project of Jilin Province (Grant No. 20200801059 GH).

References

[1] S. Gao, G. Wang, L. Guo, S. Yu, Tunable and ultraefficient microwave absorption properties of trace N-doped two-dimensional carbon-based nanocomposites loaded with multi-rare earth oxides, Small 16 (2020) 1265–1302, https://doi.org/10.1002/smll.201906668.

[2] Y. Wang, S. Yang, H. Wang, G. Wang, X. Sun, P. Yin, Hollow porous CoNi/C composite nanomaterials derived from MOFs for efficient and lightweight electromagnetic wave absorber, Carbon 167 (2020) 485–494, https://doi.org/10.1016/j.carbon.2020.06.014.

[3] X. Cui, X. Liang, W. Liu, W. Gu, G. Ji, Y. Du, Stable microwave absorber derived from 1D customized heterogeneous structures of Fe3N@C, Chem. Eng. J 381 (2020) 122589, https://doi.org/10.1016/j.cej.2019.122589.

[4] Y. Huang, X. Zhao, M. Zong, J. Yan, T. Li, Preparation of ternary composite material rGO/$CoFe_2O_4$/Ag and research on its microwave absorption properties, J. Mater. Sci. Mater. Electron 32 (2021) 23944–23957, https://doi.org/10.1007/s10854-021-06856-9.

[5] B. Quan, W. Shi, S.J.H. Ong, X. Lu, P.L. Wang, G. Ji, Y. Guo, L. Zheng, Z.J. Xu, Defect engineering in two common types of dielectric materials for electromagnetic absorption applications, Adv. Funct. Mater. 29 (2019), 1901636, https://doi.org/10.1002/adfm.201901236.

[6] L. Ding, X. Zhao, Y. Huang, J. Yan, T. Li, P. Liu, Ultra-broadband and covalently linked core-shell $CoFe_2O_4$@PPy nanoparticles with reduced graphene oxide for microwave absorption, J. Colloid Interface Sci. 595 (2021) 168–177, https://doi.org/10.1016/j.jcis.2021.03.019.

[7] X. Hu, H. Nan, M. Liu, S. Liu, T. An, H. Tian, Battery-like $MnCo_2O_4$ electrode materials combined with active carbon for hybrid supercapacitors, Electrochim. Acta 306 (2019) 599–609, https://doi.org/10.1016/j.electacta.2019.03.166.

[8] X. Lang, H. Zhang, X. Xue, C. Li, X. Sun, Z. Liu, H. Nan, X. Hu, H. Tian, Rational design of $La_{0.85}Sr_{0.15}MnO_3$@$NiCo_2O_4$ Core-Shell architecture supported on Ni foam for high performance supercapacitors, J. Power Sources 402 (2018) 213–220, https://doi.org/10.1016/j.jpowsour.2018.09.040.

[9] H. Tian, X. Lang, H. Nan, P. An, W. Zhang, X. Hu, J. Zhang, Nanosheet-assembled $LaMnO_3$@$NiCo_2O_4$ nanoarchitecture growth on Ni foam for high power density supercapacitors, Electrochim. Acta 318 (2019) 651–659, https://doi.org/10.1016/j.electacta.2019.06.133.

[10] L. Wang, Y. Wang, H. Tian, L. Qiao, Y. Zeng, Enhanced ammonia detection using wrinkled porous $CoFe_2O_4$ double-shelled spheres prepared by a thermally driven contraction process, Sens. Actuators B Chem. 314 (2020), 128085, https://doi.org/10.1016/j.snb.2020.128085.

[11] S. Gao, S. Yang, H. Wang, G. Wang, P. Yin, Excellent electromagnetic wave absorbing properties of two-dimensional carbon-based nanocomposite supported by transition metal carbides Fe_3C, Carbon 162 (2020) 438–444, https://doi.org/10.1016/j.carbon.2020.02.031.

[12] X. Liu, X. Zhao, J. Yan, Y. Huang, T. Li, P. Liu, Enhanced electromagnetic wave absorption performance of core-shell Fe_3O_4@poly(3,4-ethylenedioxythiophene) microspheres/reduced graphene oxide composite, Carbon 178 (2021) 273–284, https://doi.org/10.1016/j.carbon.2021.03.042.

[13] X. Wang, T. Ma, J. Shu, M. Cao, Confinedly tailoring Fe_3O_4 clusters-NG to tune electromagnetic parameters and microwave absorption with broadened bandwidth, Chem. Eng. J 332 (2018) 321–330, https://doi.org/10.1016/j.cej.2017.09.101.

[14] M. Zong, Y. Huang, N. Zhang, Reduced graphene oxide-$CoFe_2O_4$ composite: synthesis and electromagnetic absorption properties, Appl. Surf. Sci. 345 (2015) 272–278, https://doi.org/10.1016/j.apsusc.2015.03.203.

[15] M. Zong, Y. Huang, Y. Zhao, X. Sun, C. Qu, D. Luo, J. Zheng, Facile preparation, high microwave absorption and microwave absorbing mechanism of RGO-Fe_3O_4 composites, RSC Adv. 3 (2013) 23638–23648, https://doi.org/10.1039/c3ra43359e.

[16] X. Huang, G. Yu, Y. Zhang, M. Zhang, G. Shao, Design of cellular structure of graphene aerogels for electromagnetic wave absorption, Chem. Eng. J 426 (2021), 131894, https://doi.org/10.1016/j.cej.2021.131894.

[17] K.L. Zhang, J. Chen, S.J. Yue, H.Y. Zhang, C. Meng, J.G. Wang, Facile synthesis of core-shell CI/SiO_2 decorated RGO sheets composite for excellent electromagnetic wave absorption performance covering the whole X-band, Compos. Part A Appl. Sci. Manuf 130 (2020), 105755, https://doi.org/10.1016/j.compositesa.2019.105755.

[18] H. Wang, H. Tian, X. Wang, L. Qiao, S. Wang, X. Wang, W. Zheng, Y. Liu, Electrical conductivity of alkaline-reduced graphene oxide, Chem. Res. Chin. Univ. 27 (2011) 857–861. http://crcu.jlu.edu.cn/EN/Y2011/V27/I5/857.

[19] X. Zhao, Y. Huang, X. Liu, J. Yan, L. Ding, M. Zong, P. Liu, T. Li, Core-shell $CoFe_2O_4$@C nanoparticles coupled with rGO for strong wideband microwave absorption, J. Colloid Interface Sci. 607 (2022) 192–202, https://doi.org/10.1016/j.jcis.2021.08.203.

[20] X.Y. Wang, Y.K. Lu, T. Zhu, S.C. Chang, W. Wang, $CoFe_2O_4$/N-doped reduced graphene oxide aerogels for high-performance microwave absorption, Chem. Eng. J 388 (2020), 124317, https://doi.org/10.1016/j.cej.2020.124317.

[21] T. Zhu, S.C. Chang, Y.F. Song, M. Lahoubi, W. Wang, PVP-encapsulated $CoFe_2O_4$/rGO composites with controllable electromagnetic wave absorption performance, Chem. Eng. J 373 (2019) 755–766, https://doi.org/10.1016/j.cej.2019.05.079.

[22] X. Tao, Y. Li, J. Du, Y. Xia, Y. Yang, H. Huang, Y. Gan, W. Zhang, X. Li, A generic bamboo-based carbothermal method for preparing carbide (SiC, B_4C, TiC, TaC, NbC, $Ti_xNb_{1-x}C$, and $Ta_xNb_{1-x}C$) nanowires, J. Mater. Chem. 21 (2011) 9095–9102, https://doi.org/10.1039/c1jm10730e.

[23] L. Ma, M. Hamidinejad, B. Zhao, C. Liang, C.B. Park, Layered foam/film polymer nanocomposites with highly efficient EMI shielding properties and ultralow reflection, Nano-Micro Lett. 14 (2022) 19, https://doi.org/10.1007/s40820-021-00759-4.

[24] G. Zeng, X. Li, Y. Wei, T. Guo, X. Huang, X. Chen, X. Tang, Significantly toughened SiC foams with enhanced microwave absorption via in situ growth of Si3N4 nanowires, Chem. Eng. J 426 (2021), 131745, https://doi.org/10.1016/j.cej.2021.131745.

[25] Y. Zhou, M. Wu, J. Jiang, P. Yang, T. Rao, J.J. Liou, W. Liao, Self-assembling SiC nanoflakes/MXenes composites embedded in polymers towards efficient electromagnetic wave attenuation, Appl. Surf. Sci. 574 (2022), 151463, https://doi.org/10.1016/j.apsusc.2021.151463.

[26] W.Q. Yang, D. Yang, H. Mei, L. Yao, S.S. Xiao, Y.T. Yao, C. Chen, L.F. Cheng, 3D printing of PDC-SiOC@SiC twins with high permittivity and electromagnetic interference shielding effectiveness, J. Eur. Ceram. Soc. 41 (2021) 5437–5444, https://doi.org/10.1016/j.jeurceramsoc.2021.04.048.

[27] Z. Gao, W. Yang, J. Wang, N. Song, X. Li, Flexible all-solid-state hierarchical $NiCo_2O_4$/porous graphene paper asymmetric supercapacitors with an exceptional combination of electrochemical properties, Nano Energy 13 (2015) 306–317, https://doi.org/10.1016/j.nanoen.2015.02.036.

[28] N. Song, Z. Gao, Y. Zhang, X. Li, B_4C nanoskeleton enabled, flexible lithium-sulfur batteries, Nano Energy 58 (2019) 30–39, https://doi.org/10.1016/j.nanoen.2019.01.018.

[29] Z. Gao, N. Song, X. Li, Microstructural design of hybrid CoO@NiO and graphene nano-architectures for flexible high performance supercapacitors, J. Mater. Chem. A3 (2015) 14833–14844, https://doi.org/10.1039/c5ta03057a.

[30] B. Huang, Z. Wang, H. Hu, X. Tang, X. Huang, J. Yue, Y. Wang, Enhancement of the microwave absorption properties of PyC-SiC_f/SiC composites by electrophoretic deposition of SiC nanowires on SiC fibers, Ceram. Int. 46 (2020) 9303–9310, https://doi.org/10.1016/j.ceramint.2019.12.185.

[31] P. Liu, Y. Huang, X. Zhang, Synthesis of graphene@branching-like polypyrrole@$CoFe_2O_4$ composites and their excellent electromagnetic wave absorption properties, Mater. Lett. 136 (2014) 298–301, https://doi.org/10.1016/j.matlet.2014.08.024.

[32] H. Liu, M. Zhang, Y. Ye, J. Yi, Y. Zhang, Q. Liu, Porous cobalt ferrite microspheres decorated two-dimensional MoS_2 as an efficient and wideband microwave absorber, J. Alloys Compd. 892 (2022), 162126, https://doi.org/10.1016/j.jallcom.2021.162126.
[33] Y. Wang, Y. Li, H. Luo, Z. Li, Z. Li, W. Zhou, P. Xiao, Improved microwave absorption properties of polycarbosilane-derived SiC core-shell particles by oxidation, J. Alloys Compd. 786 (2019) 409–417, https://doi.org/10.1016/j.jallcom.2019.01.337.
[34] N. Song, Z. Gao, X. Li, Tailoring nanocomposite interfaces with graphene to achieve high strength and toughness, Sci. Adv. 6 (2020) 48, https://doi.org/10.1126/sciadv.aba7016.
[35] Y. Zhang, X. Li, Bioinspired, graphene/Al_2O_3 doubly reinforced aluminum composites with high strength and toughness, Nano Lett. 17 (2017) 6907–6915, https://doi.org/10.1021/acs.nanolett.7b03308.
[36] Y. Jia, X. Xiong, D. Wang, X. Duan, K. Sun, Y. Li, L. Zheng, W. Lin, M. Done, G. Zhang, W. Liu, X. Sun, Atomically dispersed Fe-N_4 modified with precisely located S for highly efficient oxygen reduction, Nano-Micro Lett. 12 (2020) 116, https://doi.org/10.1007/s40820-020-00456-8.
[37] C. Han, M. Zhang, W. Cao, M. Cao, Electrospinning and in-situ hierarchical thermal treatment to tailor C-$NiCo_2O_4$ nanofibers for tunable microwave absorption, Carbon 171 (2021) 953–962, https://doi.org/10.1016/j.carbon.2020.09.067.
[38] Y. Cheng, J.Z.Y. Seow, H. Zhao, Z.J. Xu, G. Ji, A flexible and lightweight biomass-reinforced microwave absorber, Nano-Micro Lett. 12 (2020) 125, https://doi.org/10.1007/s40820-020-00461-x.
[39] W. Gu, J. Sheng, Q. Huang, G. Wang, J. Chen, G. Ji, Environmentally friendly and multifunctional shaddock peel-based carbon aerogel for thermal-insulation and microwave absorption, Nano-Micro Lett. 13 (2021) 102, https://doi.org/10.1007/s40820-021-00635-1.
[40] P. Liu, S. Gao, Y. Wang, Y. Huang, F. Zhou, P. Liu, Magnetic porous N-doped carbon composites with adjusted composition and porous microstructure for lightweight microwave absorbers, Carbon 173 (2021) 655–666, https://doi.org/10.1016/j.carbon.2020.11.043.
[41] M. Ma, Z. Liao, X. Su, Q. Zheng, Y. Liu, Y. Wang, Y. Ma, F. Wan, Magnetic CoNi alloy particles embedded N-doped carbon fibers with polypyrrole for excellent electromagnetic wave absorption, J. Colloid Interface Sci. 608 (2021) 2203–2212, https://doi.org/10.1016/j.jcis.2021.10.006.
[42] X. Cui, X. Liang, J. Chen, W. Gu, G. Ji, Y. Du, Customized unique core-shell Fe_2N@N-doped carbon with tunable void space for microwave response, Carbon 156 (2020) 49–57, https://doi.org/10.1016/j.carbon.2019.09.041.
[43] B. Quan, W. Gu, J. Sheng, X. Lv, Y. Mao, L. Liu, X. Huang, Z. Tian, G. Ji, From intrinsic dielectric loss to geometry patterns: dual-principles strategy for ultrabroad band microwave absorption, Nano Res. 14 (2021) 1495–1501, https://doi.org/10.1007/s12274-020-3208-8.
[44] X. Wang, W. Cao, M. Cao, J. Yuan, Assembling nano-microarchitecture for electromagnetic absorbers and smart devices, Adv. Mater. 32 (2020), 2002122, https://doi.org/10.1002/adma.202002112.
[45] S. Gao, G. Zhang, Y. Wang, X. Han, Y. Huang, P. Liu, MOFs derived magnetic porous carbon microspheres constructed by core-shell Ni@C with high-performance microwave absorption, J. Mater. Sci. Technol. 88 (2021) 56–65, https://doi.org/10.1016/j.jmst.2021.02.011.
[46] J.L. Luo, H. Guo, J. Zhou, F. Guo, G.G. Liu, G.Z. Hao, W. Jiang, Rational construction of heterogeneous interfaces for bimetallic MOFs-derived/rGO composites towards optimizing the electromagnetic wave absorption, Chem. Eng. J 429 (2022), 132238, https://doi.org/10.1016/j.cej.2021.132238.
[47] Z. Tong, Y. Bi, M. Ma, Z. Liao, W. Huang, K.L. Chung, Y. Ma, G. Wu, Y. Qu, C. Pan, Y. Wang, Fabrication of flower-like surface Ni@Co_3O_4 nanowires anchored on RGO nanosheets for high-performance microwave absorption, Appl. Surf. Sci. 565 (2021), 150483, https://doi.org/10.1016/j.apsusc.2021.150483.
[48] P. Liu, S. Gao, Y. Wang, F. Zhou, Y. Huang, W. Huang, N. Chang, Core-shell Ni@C encapsulated by N-doped carbon derived from nickel-organic polymer coordination composites with enhanced microwave absorption, Carbon 170 (2020) 503–516, https://doi.org/10.1016/j.carbon.2020.08.043.
[49] M. Cao, X. Wang, M. Zhang, J. Shu, W. Cao, H. Yang, X. Fang, J. Yuan, Electromagnetic response and energy conversion for functions and devices in low-dimensional materials, Adv. Funct. Mater. 29 (2019), 1807398, https://doi.org/10.1002/adfm.201807398.
[50] P. Liu, Y. Zhang, J. Yan, Y. Huang, L. Xia, Z. Guang, Synthesis of lightweight N-doped graphene foams with open reticular structure for high-efficiency electromagnetic wave absorption, Chem. Eng. J 368 (2019) 285–298, https://doi.org/10.1016/j.cej.2019.02.193.
[51] Y. Duan, H. Pang, X. Wen, X. Zhang, T. Wang, Microwave absorption performance of $FeCoNiAlCr_{0.9}$ alloy powders by adjusting the amount of process control agent, J. Mater. Sci. Technol. 77 (2021) 209–216, https://doi.org/10.1016/j.jmst.2020.09.049.
[52] L. Huang, Y. Duan, X. Dai, Y. Zeng, G. Ma, Y. Liu, S. Gao, W. Zhang, Bioinspired metamaterials: multibands electromagnetic wave adaptability and hydrophobic characteristics, Small 15 (2019), 1902730, https://doi.org/10.1002/smll.201902730.
[53] X. Yang, Y. Duan, Y. Zeng, H. Pang, G. Ma, X. Dai, Experimental and theoretical evidence for temperature driving an electric-magnetic complementary effect in magnetic microwave absorbing materials, J. Mater. Chem. C 8 (2020) 1583–1590, https://doi.org/10.1039/c9tc06551b.
[54] Y. Duan, H. Pang, H. Zhang, Structure and composition design on ternary CNT@ZnFe2O4@ZnO composite utilized as enhanced microwave absorbing materials, Diam. Relat. Mater. 120 (2021), 108701, https://doi.org/10.1016/j.diamond.2021.108701.
[55] H. Pang, Y. Duan, L. Huang, L. Song, J. Liu, T. Zhang, X. Yang, J. Liu, X. Ma, J. Di, X. Liu, Research advances in composition, structure and mechanisms of microwave absorbing materials, Compos. B Eng. 224 (2021), 109173, https://doi.org/10.1016/j.compositesb.2021.109173.
[56] X. Chen, Y. Wang, H. Liu, S. Jin, G. Wu, Interconnected magnetic carbon@NixCo(1-x)Fe(2)O(4) nanospheres with core-shell structure: an efficient and thin electromagnetic wave absorber, J. Colloid Interface Sci. 606 (2022) 526–536, https://doi.org/10.1016/j.jcis.2021.07.094.
[57] L. Liang, W. Gu, Y. Wu, B. Zhang, G. Wang, Y. Yang, G. Ji, Heterointerface engineering in electromagnetic absorbers: new insights and opportunities, Adv. Mater. 34 (2021), 2106195, https://doi.org/10.1002/adma.202106195.
[58] P. Liu, S. Gao, Y. Wang, Y. Huang, Y. Wang, J. Luo, Core-shell CoNi@graphitic carbon decorated on B,N-codoped hollow carbon polyhedrons toward lightweight and high-efficiency microwave attenuation, ACS Appl. Mater. Interfaces 11 (2019) 25624–25635, https://doi.org/10.1021/acsami.9b08525.
[59] X. Zhang, L. Xia, B. Zhong, H. Yang, B. Shi, L. Huang, Y. Yang, X. Huang, Three-dimensional reduced graphene oxide/$CoFe_2O_4$ composites loaded with LAS particles for lightweight and enhanced microwave absorption properties, J. Alloys Compd. 799 (2019) 368–376, https://doi.org/10.1016/j.jallcom.2019.05.281.
[60] J. Shu, M. Cao, M. Zhang, X. Wang, W. Cao, X. Fang, M. Cao, Molecular patching engineering to drive energy conversion as efficient and environment-friendly cell toward wireless power transmission, Adv. Funct. Mater. 30 (2020), 1908299, https://doi.org/10.1002/adfm.201908299.
[61] X. Zhang, J. Zhu, P. Yin, A. Guo, A. Huang, L. Guo, G. Wang, Tunable high-performance microwave absorption of $Co_{1-x}S$ hollow spheres constructed by nanosheets within ultralow filler loading, Adv. Funct. Mater. 28 (2018), 1800761, https://doi.org/10.1002/adfm.201800761.
[62] M. Zhang, C. Han, W. Cao, M. Cao, H. Yang, J. Yuan, A nano-micro engineering nanofiber for electromagnetic absorber, green shielding and sensor, Nano-Micro Lett. 13 (2021) 27, https://doi.org/10.1007/s40820-020-00552-9.
[63] X. Liu, X. Lu, H. Guan, X. Liu, M. Wang, C. Wang, D. Zhao, Z. Xia, Rational design of ZnO/ZnO nanocrystal-modified rGO foam composites with wide-frequency microwave absorption properties, Ceram. Int. 47 (2021) 33584–33595, https://doi.org/10.1016/j.ceramint.2021.08.268.
[64] C. Wang, Z. Huang, J. Zhou, M. Song, X. Chen, Y. Zheng, C. Yang, W. Xia, W. Xia, One-step synthesis of SiC/C nanocomposites by atmospheric thermal plasmas for efficient microwave absorption, Ceram. Int. 48 (2022) 10391–10402, https://doi.org/10.1016/j.ceramint.2021.12.106.
[65] Y. Liu, Z. Chen, Y. Zhang, R. Feng, X. Chen, C. Xiong, L. Dong, Broadband and lightweight microwave absorber constructed by in situ growth of hierarchical $CoFe_2O_4$/reduced graphene oxide porous nanocomposites, ACS Appl. Mater. Interfaces 10 (2018) 13860–13868, https://doi.org/10.1021/acsami.8b02137.
[66] R. Jaiswal, K. Agarwal, V. Pratap, A. Soni, S. Kumar, K. Mukhopadhyay, N. E. Prasad, Microwave-assisted preparation of magnetic ternary core-shell nanofiller ($CoFe_2O_4$/rGO/SiO_2) and their epoxy nanocomposite for microwave absorption properties, Mat. Sci. Eng. B-Adv. 262 (2020), 114711, https://doi.org/10.1016/j.mseb.2020.114711.
[67] Z. Liu, Z. Xiang, B. Deng, F. Pan, J. Xiong, W. Lu, Rational design of hierarchical porous Fe_3O_4/rGO composites with lightweight and high-efficiency microwave absorption, Compos. Commun. 22 (2020), 100492, https://doi.org/10.1016/j.coco.2020.100492.
[68] Y. Fan, D. Yang, H. Mei, S. Xiao, Y. Yao, L. Cheng, L. Zhang, Tuning SiC nanowires interphase to improve the mechanical and electromagnetic wave absorption properties of SiC_f/SiC_{nw}/Si_3N_4 composites, J. Alloys Compd. 896 (2022), 163017, https://doi.org/10.1016/j.jallcom.2021.163017.